Nanoscale

PAPER

View Article Online
View Journal | View Issue

Cite this: *Nanoscale*, 2017, **9**, 1942

Carbon/two-dimensional $MoTe_2$ core/shell-structured microspheres as an anode material for Na-ion batteries†

Jung Sang Cho,[a,b] Hyeon Seok Ju,[a] Jung-Kul Lee*[c] and Yun Chan Kang*[a]

Unique-structured composite microspheres of carbon and $MoTe_2$ were prepared by a two-step process. Precursor C–MoO_x composite microspheres were prepared by spray pyrolysis, and then the precursor was transformed into C–$MoTe_2$ composite microspheres by a tellurization process. C–$MoTe_2$ composites with a uniform distribution of $MoTe_2$ nanocrystals (C/$MoTe_2$) and core–shell-structured C–$MoTe_2$ composites (C@$MoTe_2$) were synthesized at tellurization temperatures of 450 and 600 °C, respectively. At a higher tellurization temperature of 600 °C, all of the $MoTe_2$ nanocrystals moved to the surface of the microsphere because of the Ostwald ripening process. The initial discharge capacities of the C/$MoTe_2$, C@$MoTe_2$, and bare $MoTe_2$ (*i.e.*, containing no carbonaceous materials) powders for Na-ion storage at a current density of 1.0 A g^{-1} were 328, 388, and 341 mA h g^{-1}, respectively. The discharge capacities of the C/$MoTe_2$, C@$MoTe_2$, and bare $MoTe_2$ powders for the 200th cycle were 241, 286, and 104 mA h g^{-1}, respectively, and the corresponding capacity retentions, which were measured from the second cycle were 100%, 99%, and 37%, respectively. The high structural stability and well-developed two-dimensional layer of $MoTe_2$ of the C@$MoTe_2$ microspheres provide superior Na-ion storage properties compared to those of the C/$MoTe_2$ microspheres and bare $MoTe_2$ powder.

Received 9th September 2016,
Accepted 27th December 2016

DOI: 10.1039/c6nr07158a

rsc.li/nanoscale

Introduction

Two-dimensional (2D) materials composed of transition metals, whose crystal structure results from the stacking of sheets of packed atoms, have been widely studied because of their distinctive electronic, optical, catalytic, and electrochemical properties.[1–5] In particular, 2D transition-metal sulfides and selenides that are structurally similar to graphite are of great interest as energy storage and conversion materials, such as Li-air batteries, Li- and Na-ion batteries (LIBs and NIBs, respectively), and in hydrogen-evolution reactions (HERs).[6–10]

Recently, NIBs have been considered as the next generation of rechargeable batteries for large-scale energy storage because of their environmental friendliness and low cost.[11–15] Transition metal chalcogenides (MY_x, where M = Fe, Sn, Co, and Mo, and Y = S and Se) have good characteristics for anode materials in NIBs.[14,16–22] Among these materials, the Mo-based dichalcogenides MoS_2 and $MoSe_2$ have been applied to NIBs because of their unique sandwich structure, which is composed of alternately stacked layers of Mo and S or Se (*i.e.*, S–Mo–S and Se–Mo–Se, respectively).[10,21–24] In addition, such materials can be prepared by various liquid-solution and gas-phase reaction processes.[21–23] The unique layer-by-layer structure allows for the sodiation and desodiation of Na ions between the layers.[10] However, the electrochemical properties of MoS_2 and $MoSe_2$ need enhancement in terms of cycling properties, which are generally related to the structural stability of materials, for application as anode materials in NIBs. The structural instabilities may be due to the small interlayer distance and large structural resistance against Na-ion sodiation. Therefore, it is imperative to explore new materials that could be used as anode materials in NIBs.

$MoTe_2$, which belongs to the family of 2D Mo-based materials, is composed of alternately stacked layers of Mo and Te (*i.e.*, Te–Mo–Te) that are held together by weak van der Waals interactions.[25–28] Both single- and few-layer $MoTe_2$ exhibit narrow band gaps and such materials have been studied for applications in electronic devices and photoelectrochemical cells.[27–29] However, to the best of our knowledge, the

[a]*Department of Materials Science and Engineering, Korea University, Anam-Dong, Seongbuk-Gu, Seoul 136-713, Republic of Korea. E-mail: yckang@korea.ac.kr; Fax: (+82) 2-928-3584*
[b]*Department of Engineering Chemistry, Chungbuk National University, Chungbuk 361-763, Republic of Korea*
[c]*Department of Chemical Engineering, Konkuk University, 1 Hwayang-dong, Gwangjin-gu, Seoul 143-701, Republic of Korea*
†Electronic supplementary information (ESI) available. See DOI: 10.1039/c6nr07158a

synthesis of nanostructured $MoTe_2$ materials that contain carbonaceous materials and the electrochemical properties of $MoTe_2$ as energy storage materials in LIBs and NIBs have not been studied. The interlayer spacing of $MoTe_2$ is 0.699 nm, which is significantly larger than that of graphite (0.335 nm) and slightly larger than that of MoS_2 (0.615 nm) and $MoSe_2$ (0.646 nm).[30–33] The large interlayer spacing and weak van der Waals interactions between the $MoTe_2$ layers are expected to allow the efficient diffusion of the massive Na ions without any significant changes in the volume. Moreover, tellurium has a substantially higher electronic conductivity (2×10^2 S m^{-1}), resulting in higher utilization of active materials compared with sulfur (5×10^{-28} S m^{-1}) and selenium (1×10^{-3} S m^{-1}). Hence, $MoTe_2$ could be developed as an intercalation host, and thus, it is a very promising electrode material for NIBs.

In this study, to the best of our knowledge, carbon (C)–$MoTe_2$ composite microspheres were prepared for the first time by a simple two-step process. Precursor C–MoO_x composite microspheres were prepared by spray pyrolysis and then transformed into C–$MoTe_2$ composite microspheres by a simple tellurization process. C–$MoTe_2$ composite microspheres with a uniform distribution of $MoTe_2$ nanocrystals (C/$MoTe_2$) and core–shell-structured C–$MoTe_2$ microspheres (C@$MoTe_2$) were synthesized at tellurization temperatures of 450 and 600 °C, respectively. The formation mechanisms and electrochemical properties of the two types of C–$MoTe_2$ composite microspheres were investigated.

Experimental section

Sample preparation

The precursor C–MoO_x composite microspheres used to fabricate the C–$MoTe_2$ composite microspheres were prepared by a one-pot spray pyrolysis process. The details of the spray pyrolysis system used are shown in Fig. S1,† and the system was described in detail in our previous papers. In brief, droplets were generated with a 1.7 MHz ultrasonic spray generator that consisted of six vibrators, and the droplets were carried to a quartz tube reactor (length = 1200 mm, diameter = 50 mm) by a flow of N_2 gas (flow rate = 10 L min^{-1}). The reactor temperature was fixed at 500 °C. The spray solution was prepared by dissolving 0.1 M of MoO_3 (Sigma Aldrich, 98%) and 0.1 M of sucrose, which was used as the source of C. To prepare the C/$MoTe_2$ composite microspheres with a homogeneous distribution of $MoTe_2$ nanocrystals, the as-prepared precursor C–MoO_x composite microspheres were tellurized at 450 °C for 12 h under a reducing atmosphere of 10% H_2 and Ar with powdered Te. H_2Te gas was formed from the powdered Te *via* the following reaction with H_2 gas: Te (s) + H_2 (g) → H_2Te (g). For the tellurization process, an alumina boat containing the C–MoO_x composite microspheres was loaded into a larger, covered alumina boat. The powdered Te was placed outside of the smaller alumina boat. A tellurization process was also performed at 600 °C to obtain the core–shell-structured C@$MoTe_2$ microspheres. For comparison purposes, bare $MoTe_2$ microspheres, *i.e.*, $MoTe_2$ microspheres that did not contain carbonaceous materials, were also prepared. In this case, the precursor C–MoO_x composite microspheres were post-treated at 400 °C for 3 h under an air atmosphere for decomposition of the carbonaceous materials. The subsequent tellurization of the MoO_3 powder at 600 °C for 6 h in H_2Te gas produced the bare $MoTe_2$ powder. For simplicity, the C/$MoTe_2$ composite microspheres with a homogeneous distribution of $MoTe_2$ nanocrystals, core–shell-structured C@$MoTe_2$ microspheres, and bare $MoTe_2$ microspheres will hereinafter be referred to as "C/$MoTe_2$", "C@$MoTe_2$", and "bare $MoTe_2$", respectively.

Characterization

The crystal structures of the C–MoO_3 and C–$MoTe_2$ composite microspheres were investigated by X-ray diffraction (XRD, X'pert PRO MPD; Cu-K_α radiation, λ = 1.5418 Å), which was performed at the Korea Basic Science Institute (Daegu). The morphologies of the samples were observed by scanning electron microscopy (SEM, TESCAN VEGA3 SBH) and high-resolution transmission electron microscopy (HR-TEM, JEOL JEM-2100F) at a working voltage of 200 kV. X-ray photoelectron spectroscopy (XPS, Thermo Scientific, K-Alpha) was performed on the samples with Al-K_α radiation (1486.6 eV). The structure of the carbonaceous materials in the microspheres was characterized *via* Raman spectroscopy (Jobin Yvon LabRam, HR800, excitation source = 632.8 nm He–Ne laser) at room temperature. To determine the C content of the C–$MoTe_2$ composite microspheres, thermogravimetric analysis (TGA, Perkin Elmer, SDT Q600) was performed in air at a heating rate of 10 °C min^{-1}. The surface areas of the microspheres were determined with the Brunauer–Emmett–Teller (BET) method, where N_2 was the adsorbate gas.

Electrochemical measurements

The electrochemical properties of the C–$MoTe_2$ composite microspheres were analyzed using a 2032-type coin cell. The anode was prepared by mixing the active material, carbon black, and sodium carboxymethyl cellulose (CMC) in a weight ratio of 7 : 2 : 1, respectively. Na metal and a microporous polypropylene film were used as the counter electrode and the separator, respectively. The electrolyte was prepared by dissolving 1 M of $NaClO_4$ and 5% of fluoroethylene carbonate (FEC) in a mixture of ethylene carbonate and dimethyl carbonate (EC and DMC, respectively; 1 : 1 v/v). The discharge/charge characteristics of the samples were investigated by cycling over a potential range of 0.001–3.0 V at various current densities. Cyclic voltammograms (CVs) were measured at a scan rate of 0.07 mV s^{-1}. The size of the negative electrode containing the $MoTe_2$ powder was 1.5 cm × 1.5 cm, and the mass loading was approximately 2.0 mg cm^{-2}. In this study, the capacities of the samples were calculated based on the total mass of the $MoTe_2$/carbon composite. Electrochemical impedance spectra were obtained by performing alternating-current electrochemical impedance spectroscopy (EIS, ZIVE SP1) over a frequency range of 0.01 Hz to 100 kHz.

Results and discussion

The formation mechanisms of the C/$MoTe_2$ and C@$MoTe_2$ composite microspheres are shown in Scheme 1. One C–MoO_x composite microsphere, in which ultrafine MoO_x nanocrystals are uniformly distributed throughout the C microsphere, is formed from one droplet of solution by the one-pot spray pyrolysis process (Scheme 1-① and Fig. S1†). The tellurization of MoO_x by the H_2Te gas (formed from the Te powder *via* a reaction with H_2 gas, Te (s) + H_2 (g) → H_2Te (g)) produces a C–$MoTe_2$ composite microsphere by: MoO_x (s) + $2H_2Te$ (g) → $MoTe_2$ (s) + yH_2O (g) + $2H_2$ (g). The $MoTe_2$ nanocrystals are first formed near to the surface of the C–MoO_x composite microsphere (Scheme 1-②). The $MoTe_2$ nanocrystals located near the surface of the microsphere then move to the surface of the microsphere through an Ostwald ripening process (Scheme 1-③). Therefore, a thin layer of $MoTe_2$ covers the C–$MoTe_2$ composite microsphere tellurized at 450 °C (Scheme 1-③). At a higher tellurization temperature of 600 °C, all of the $MoTe_2$ nanocrystals move to the surface of the microsphere during the Ostwald ripening process to form a core–shell-structured C@$MoTe_2$ microsphere (Scheme 1-④).

The morphology and crystal structure of the C–MoO_x composite microspheres prepared by the one-pot spray pyrolysis process are shown in Fig. S2.† The as-prepared microspheres are spherical and there appears to be negligible aggregation. The XRD pattern of the as-prepared microspheres shows a non-crystalline structure, which is due to the short residence time (as low as 8 s) of the microspheres within the reactor maintained at 500 °C. The presence of carbonaceous materials also prevents the growth of MoO_x crystals. The morphologies of the C/$MoTe_2$ composite microspheres formed at the relatively low tellurization temperature of 450 °C are shown in Fig. 1. The SEM and TEM images shown in Fig. 1a–c reveal that the morphology of the C/$MoTe_2$ composite microspheres is similar to that of the precursor C–MoO_x composite microspheres. Therefore, the tellurization process does not change the overall morphology of the as-prepared precursor microspheres. The HR-TEM image shown in Fig. 1d exhibits clear lattice fringes that are separated by 0.70 nm, which corresponds to the (002) crystal plane of the $MoTe_2$ phase. An ultrathin (approximately 5 nm thick) $MoTe_2$ film composed of

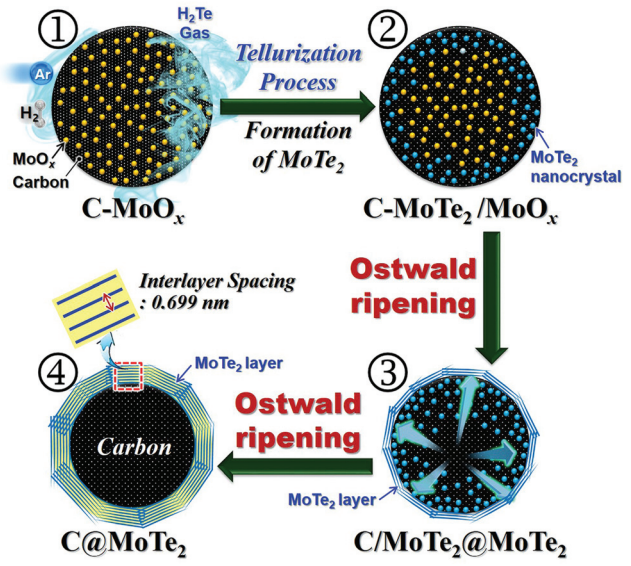

Scheme 1 Formation scheme of the C/$MoTe_2$ composite microspheres with a uniform distribution of $MoTe_2$ nanocrystals and core–shell-structured C@$MoTe_2$ composite microspheres.

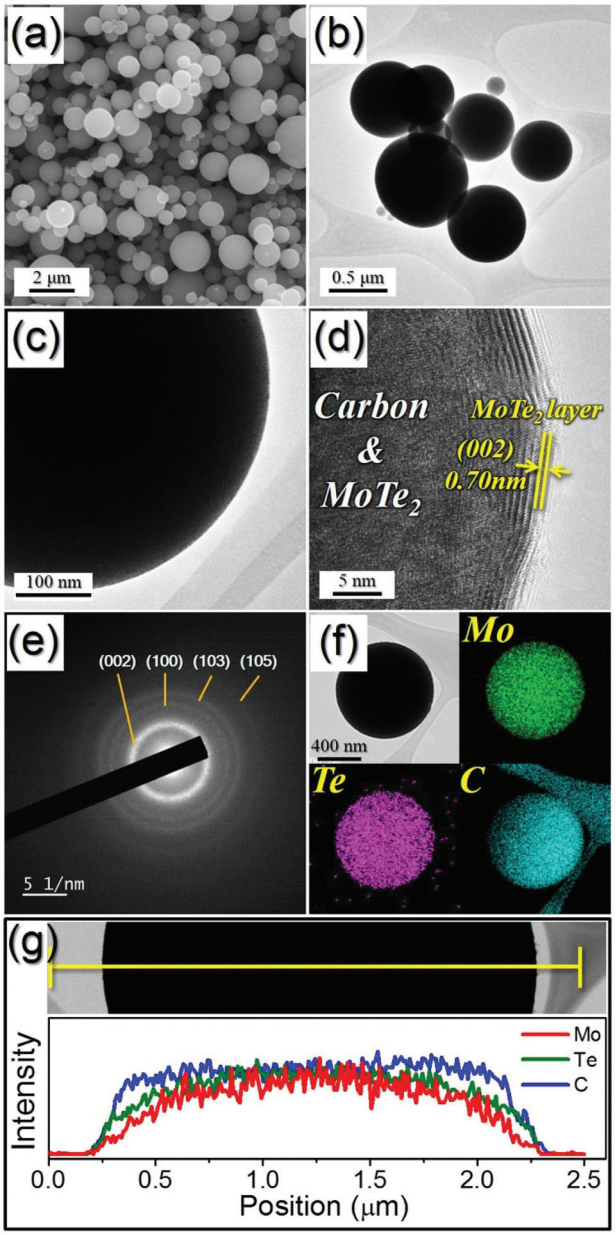

Fig. 1 Morphologies, SAED pattern, elemental mapping images, and line profiling of the C/$MoTe_2$ composite microspheres prepared by tellurization at 450 °C: (a) SEM image, (b, c) TEM images, (d) HR-TEM image, (e) SAED pattern, (f) elemental mapping images, and (g) line profiling.

Te–Mo–Te layers, which was formed by the Ostwald ripening process, covers each C/$MoTe_2$ composite microsphere. However, the inner side of the microsphere exhibits an amorphous-like structure, as shown in the HR-TEM image (Fig. 1d). EDS analysis of the composite microsphere was performed after breaking the powder for cross-sectional observation in Fig. S3.† The content of $MoTe_2$ is much higher in the outer part of the C/$MoTe_2$ composite than the inner part, as described in Scheme 1-③. Fig. S4† shows that crystalline peaks for the $MoTe_2$ phase are not present in the XRD pattern of the C–$MoTe_2$ composite microspheres. However, the selected-area electron diffraction (SAED) pattern (Fig. 1e) shows evidence of the formation of $MoTe_2$ crystals within the composite microsphere. The elemental mapping images and line profiles shown in Fig. 1f and g, respectively, confirm the formation of C/$MoTe_2$ composite microspheres. The Mo-, Te-, and C-based components are distributed throughout the C/$MoTe_2$ composite microspheres tellurized at 450 °C.

The morphologies of the C@$MoTe_2$ composite microspheres tellurized at 600 °C are shown in Fig. 2. The SEM and low-resolution TEM images shown in Fig. 1 and 2 reveal the slightly different morphologies of the C–$MoTe_2$ composite microspheres tellurized at 450 and 600 °C. Fig. 2b shows that the composite microspheres tellurized at 600 °C are covered with nanoplates, as indicated by the arrows (Fig. 2b). The HR-TEM images shown in Fig. 2c and d confirm the core–shell structure of the microspheres. The C microsphere is completely covered with highly crystalline $MoTe_2$ layers. The number of Te–Mo–Te layers covering the C microsphere shown in Fig. 2d is 24. The well-developed and clear lattice fringes on the surface are separated by 0.70 nm, which corresponds to the (002) crystal plane of the $MoTe_2$ phase. The highly stacked $MoTe_2$ layer was formed by the Ostwald ripening process, as described in Scheme 1-③; all of the ultrafine $MoTe_2$ nanocrystals that were formed inside the microsphere moved to the surface to form the highly stacked $MoTe_2$ layer during the tellurization process at 600 °C. The XRD and SAED patterns shown in Fig. S4† and Fig. 2e, respectively, also confirm the formation of highly crystalline $MoTe_2$ layers at the tellurization temperature of 600 °C. In addition, the elemental mapping images and line profiles shown in Fig. 2f and g, respectively, confirm the formation of core–shell-structured C@$MoTe_2$ composite microspheres. The mean size of the C@$MoTe_2$ composite microspheres is 1.2 μm, as measured from the SEM images. Fig. 2f shows that the Mo- and Te-based components comprising the $MoTe_2$ shell are located at the surface of the composite microsphere, as indicated by the arrows.

The chemical state and molecular environment of the C@$MoTe_2$ composite microspheres were characterized *via* XPS, as shown in Fig. 3a–d. The survey XPS spectrum (Fig. 3a) indicates the presence of Mo, Te, C, and O in the C@$MoTe_2$ composite microspheres, which is consistent with the energy dispersive X-ray spectroscopy (EDS) results (Fig. S5†). In the Mo 3d spectrum of the C@$MoTe_2$ composite microspheres (Fig. 3b), the main peaks are located at binding energies of 231.2 eV for Mo $3d_{3/2}$ and 228.1 eV for Mo $3d_{5/2}$; these are

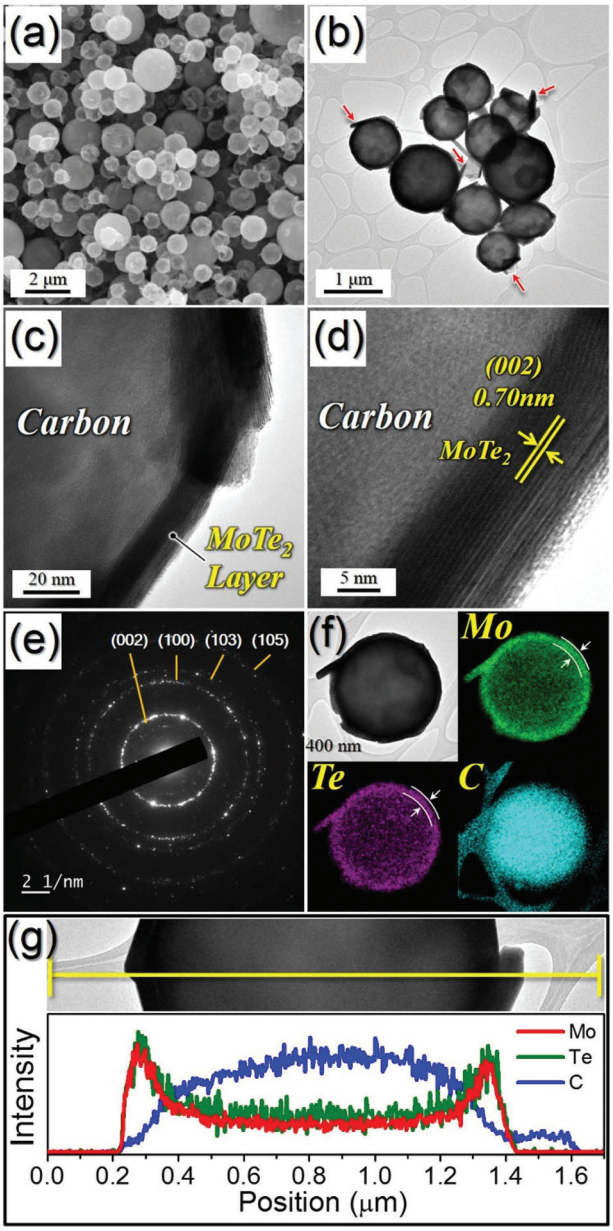

Fig. 2 Morphologies, SAED pattern, elemental mapping images, and line profiling of the core–shell structured C@$MoTe_2$ composite microspheres prepared by tellurization at 600 °C: (a) SEM image, (b, c) TEM images, (d) HR-TEM image, (e) SAED pattern, (f) elemental mapping images, and (g) line profiling.

characteristic of the $MoTe_2$ phase.[34,35] The presence of another XPS peak at 235.3 eV is attributed to the Mo $3d_{5/2}$ state of MoO_3, which may be the result of the sample undergoing surface oxidation under an air atmosphere.[36] In the Te 3d spectrum (Fig. 3c), the peaks at 572.8 and 583.1 eV correspond to Te $3d_{5/2}$ and Te $3d_{3/2}$, respectively, which are characteristic of the $MoTe_2$ phase.[34,35] In addition, two peaks are present at 576.0 and 586.5 eV, which are attributed to the presence of TeO_2 because of the exposure of the sample to air.[37] The C 1s spectrum shown in Fig. 3d exhibits peaks corresponding to

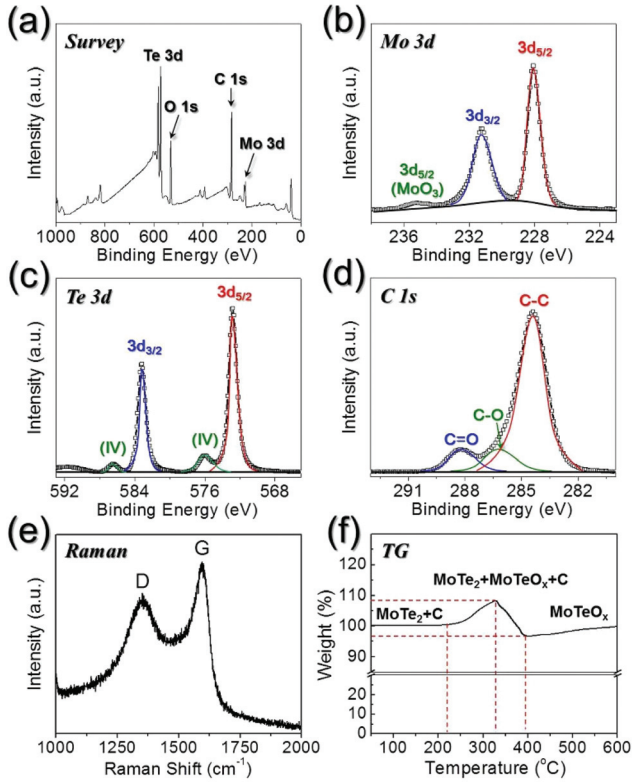

Fig. 3 XPS spectra, Raman spectrum, and the TG curve of the C@$MoTe_2$ composite microspheres prepared by tellurization at 600 °C: (a) survey XPS spectrum, (b) Mo 3d XPS spectrum, (c) Te 3d XPS spectrum, (d) C 1s XPS spectrum, (e) Raman spectrum, and (f) TG curve.

sp^2-bonded C (C–C), epoxy and alkoxy groups (C–O), and carbonyl and carboxylic components (C═O) at 284.4, 286.6, and 288.3 eV, respectively.[38–40] The Raman spectrum shown in Fig. 3e contains the characteristic wide D and G bands of C at around 1340 and 1590 cm^{-1}, respectively. The G band at 1590 cm^{-1} corresponds to the first order scattering of E_{2g} modes, *i.e.* bond stretching of all pairs of sp^2 atoms in both rings and chains.[41] The D-band is related to the defects in the graphitic carbon such as bond-angle disorder, bond-length disorder, vacancies, edge defects, *etc.*[41] In this study, the ratio of I_D/I_G for C@$MoTe_2$ composite microspheres is about 0.83, indicating the formation of graphitic carbon in the C@$MoTe_2$ microspheres. It is due to the graphitization of C occurring during the tellurization process at 600 °C. The TGA curve of the C@$MoTe_2$ composite microspheres shown in Fig. 3f exhibits a one-step weight increase and one-step weight decrease below 400 °C. The formation of $MoTeO_x$ through the oxidation of $MoTe_2$ increases the weight at approximately 300 °C in the TGA curve. The weight decrease is due to the combustion of C, which minimizes the weight increase caused by the oxidation of $MoTe_2$. The continuous formation of $MoTeO_x$ through the oxidation of $MoTe_2$ slightly increases the weight at temperatures above 400 °C in the TG curve. It is estimated that the C@$MoTe_2$ composite microspheres contain approximately 15 wt% of C, which was determined from the TGA and elemental analysis (EA) shown in Fig. 3f and Table S1,† respectively.

A bare $MoTe_2$ powder was also prepared for comparison purposes. A bare intermediate MoO_3 powder was prepared by the post-treatment of the precursor C–MoO_x composite microspheres in air. The growth of MoO_3 crystals deformed the spherical morphology of the powder formed as an intermediate product at 400 °C, as shown in Fig. S6.† The tellurization of the bare MoO_3 microspheres at 600 °C produced a phase-pure, highly crystalline, and well-facetted $MoTe_2$ powder, as shown in Fig. S6.† The highly stacked Te–Mo–Te layers were formed during the tellurization of the bare MoO_3 powder, as shown by the HR-TEM images in Fig. S7c.† The clear lattice fringes separated by 0.70 nm correspond to the (002) crystal plane of the $MoTe_2$ phase. The SAED and XRD patterns shown in Fig. S7e and S7f,† respectively, confirm the formation of a phase-pure $MoTe_2$ powder. In addition, the elemental mapping images shown in Fig. S7g† confirm the complete conversion of MoO_3 to $MoTe_2$ during the tellurization process. The BET surface areas of the C@$MoTe_2$, C/$MoTe_2$ composite microspheres and bare $MoTe_2$ powders were 42.4, 2.7, and 2.2 $m^2\ g^{-1}$, respectively. The well-developed Te–Mo–Te interlayer spacing for the C@$MoTe_2$ composite and porous carbon formed by migration of $MoTe_2$ into the surface part of the microspheres induced a high BET surface area as shown in Fig. S8.†

The electrochemical properties of the C/$MoTe_2$ and C@$MoTe_2$ composite microspheres were compared to those of the bare $MoTe_2$ powder to determine the applicability of the materials to Na-ion storage. This was achieved *via* cyclic voltammetry and galvanostatic discharge–charge cycling over a potential range of 0.001–3.0 V *vs.* Na/Na^+. The CVs of the C@$MoTe_2$ microspheres during the first five cycles at a scan rate of 0.07 mV s^{-1} are shown in Fig. 4a. A sharp reduction peak located at 0.51 V and small reduction peaks located at approximately 1.52 and 1.35 V are present in the first cathodic scan of the C@$MoTe_2$ composite microspheres. However, the Na-ion sodiation and desodiation mechanisms of $MoTe_2$ have not been identified in previous studies and therefore, the electrochemical reaction of $MoTe_2$ for Na-ion storage was estimated from that of MoS_2 and $MoSe_2$ because of their similar crystal structures.[10,21–24] During the initial discharge process, the distinct reduction peak located at approximately 0.51 V is attributed to the formation of metallic Mo nanocrystals and Na_2Te through the following conversion reaction between $MoTe_2$ and Na ions: $MoTe_2 + 4Na \rightarrow Mo + 2Na_2Te$. In order to clarify the reversible sodiation/desodiation processes of the $MoTe_2$ powders, HR-TEM images and SAED patterns were observed by disassembling the cell after full discharging and charging processes. The SAED patterns shown in Fig. 5a and b confirmed the conversion reaction process. When fully discharged, the rings in the SAED pattern were indexed to the metallic Mo and Na_2Te phases. However, the rings of the $MoTe_2$ phase were observed at a fully charged state. The HR-TEM images of the powders at fully discharged and charged states were also consistent with the above results. At

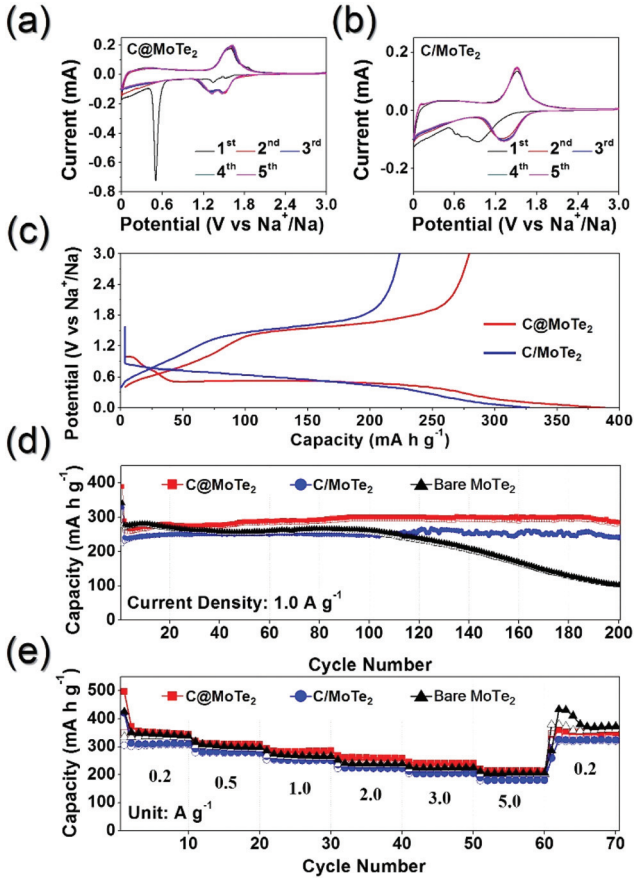

Fig. 4 CV curves of (a) C@$MoTe_2$ and (b) C/$MoTe_2$ composite microspheres scanned at a rate of 0.07 mV s^{-1}, (c) initial discharge–charge profiles, (d) cycling performances at a current density of 1.0 A g^{-1}, and (e) rate performances.

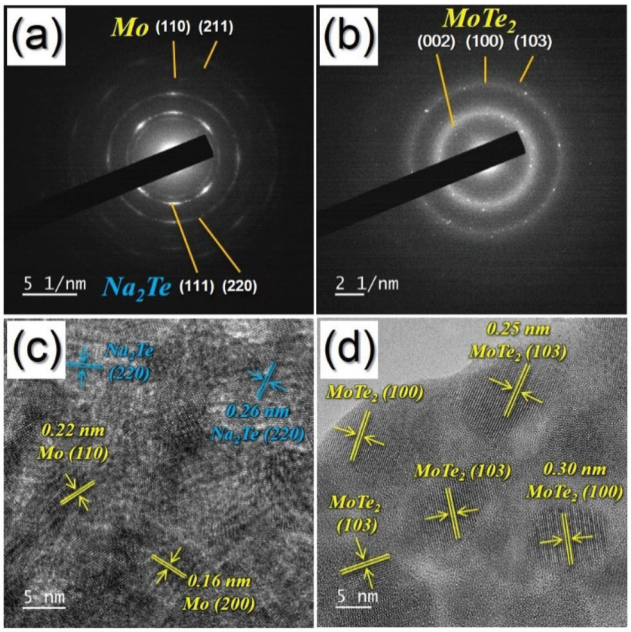

Fig. 5 SAED patterns and HR-TEM images of the C/$MoTe_2$ composite powders after the first full discharging and charging processes at a current density of 1 A g^{-1}. (a) SAED at a fully discharged state, (b) SAED at a fully charged state, (c) HR-TEM image at a fully discharged state, and (d) HR-TEM image at a fully charged state.

the fully discharged state (Fig. 5c), the lattice fringes with 0.22 nm and 0.16 nm *d*-spaces were indexed to the (110) and (200) planes of Mo metal, respectively. The interplanar spacing of 0.26 nm corresponds to the (220) plane of Na_2Te. When fully charged to 3.0 V (Fig. 5d), the (103) planes with 0.25 nm and (100) planes with 0.30 nm *d*-spaces of $MoTe_2$ were observed. The small reduction peaks located at approximately 1.52 and 1.35 V are attributed to the high crystallinity of the sintered $MoTe_2$ layers, in which the intercalation of Na ions into the Te–Mo–Te layers occurs to form Na_xMoTe_2. In contrast, the first cathodic scan of the C/$MoTe_2$ microspheres (Fig. 4b) exhibits one broad reduction peak, with the maximum peak intensity at 0.94 V. The ultrafine $MoTe_2$ nanocrystals in the C/$MoTe_2$ microspheres are responsible for this broad reduction peak. However, from the second cycle onwards, the two samples produce broad reduction peaks at similar potentials. The peak locations of the cathodic scans are shifted to higher potentials from the second cycle onwards, which is due to the formation of ultrafine $MoTe_2$ nanocrystals during the first cycle.[42,43] The HR-TEM image (Fig. 5d) confirmed the formation of ultrafine $MoTe_2$ nanocrystals during the first cycle. The broad oxidation peak located at approximately 1.51 V in the anodic scans of the two samples is due to the formation of $MoTe_2$. The discharge and charge profiles of the C/$MoTe_2$ and C@$MoTe_2$ composite microspheres at a current density of 1.0 A g^{-1} are shown in Fig. 4c. The initial discharge curve of the C@$MoTe_2$ composite microspheres exhibits two short plateaus at 0.99 and 0.76 V, and a long plateau at 0.5 V, as shown in Fig. 4c. However, the initial discharge curve of the C/$MoTe_2$ composite microspheres, which contain ultrafine nanocrystals, exhibits a long and slightly inclined plateau at approximately 0.50 V. The charge and discharge curves of the two samples are similar in shape during the second cycle. The results from the discharge and charge curves coincide well with those from the CVs. The initial discharge capacities of the C/$MoTe_2$ and C@$MoTe_2$ composite microspheres are 328 and 388 mA h g^{-1}, respectively, and the corresponding initial charge capacities are 224 and 279 mA h g^{-1}, respectively. On the other hand, the initial discharge and charge capacities of the bare $MoTe_2$ powders at a current density of 1.0 A g^{-1} (Fig. S9†) are 341 and 277 mA h g^{-1}, respectively. The initial Coulombic efficiencies of the C/$MoTe_2$ and C@$MoTe_2$ composite microspheres and bare $MoTe_2$ powders are 68, 72, and 81%, respectively. C with a high initial irreversible capacity loss in the C/$MoTe_2$ and C@$MoTe_2$ lowered the initial Coulombic efficiencies of the composite microspheres.

The cycling performances of the three samples at a current density of 1.0 A g^{-1} are shown in Fig. 4d. The C/$MoTe_2$ and C@$MoTe_2$ composite microspheres exhibit excellent cycling performances during 200 cycles despite the high current

density. In contrast, the discharge capacity of the bare $MoTe_2$ powders steadily decreases after 100 cycles. The discharge capacities of the C/$MoTe_2$, C@$MoTe_2$ and bare $MoTe_2$ samples for the 200th cycle are 241, 286, and 104 mA h g^{-1}, respectively, and the corresponding capacity retentions, which were measured from the second cycle, are 100%, 99%, and 37%, respectively. The relatively higher reversible capacities of the C@$MoTe_2$ composite microspheres and bare $MoTe_2$ powder during the first 20 cycles compared with that of the C/$MoTe_2$ microspheres are due to the well-developed Te–Mo–Te interlayer spacing, which allows Na ions to be intercalated efficiently. Thus, the high crystallinity of the $MoTe_2$ shell and incorporated C core not only enhances the specific capacities of the C@$MoTe_2$ composites, but it also improves the cyclic stabilities, which is due to the robust composite structure and the synergistic effect between the layered $MoTe_2$ shell and C core.

The rate performances of the C/$MoTe_2$ and C@$MoTe_2$, and bare $MoTe_2$ samples are shown in Fig. 4e, for which the current density was increased stepwise from 0.2 to 5.0 A g^{-1}. The samples exhibit similar rate performances, irrespective of the different internal morphologies. The final discharge capacities of the C@$MoTe_2$ composite microspheres are 343, 306, 280, 254, 236, and 209 mA h g^{-1} at current densities of 0.2, 0.5, 1.0, 2.0, 3.0, and 5.0 A g^{-1}, respectively. By considering the theoretical capacity of $MoTe_2$ (305 mA h g^{-1}; 4 mol of Na^+ for 1 mol of $MoTe_2$), the reversible capacity (approximately 345 mA h g^{-1} at 0.2 A g^{-1}) of the C@$MoTe_2$ composite microspheres exceeds the aforementioned theoretical capacity. The phenomenon of the excess capacity of $MoTe_2$ is similar to that exhibited by MoS_2 and $MoSe_2$, which is assumed to be related to the interfacial Na^+ storage, the storage of Na ions in defective sites, and the sodiation reaction of nanostructured Mo.[44,45] In addition, the synergistic effects between the well-developed 2D layer of $MoTe_2$ and C core also play a critical role in improving the excess capacity of the C@$MoTe_2$ composite microspheres.

EIS measurements were performed on the samples to investigate the superior Na-ion storage performance of the C@$MoTe_2$ composite microspheres compared to those of the other samples. The Nyquist plots (Fig. 6) of the $MoTe_2$ cells before cycling and after 1, 50, and 120 cycles were obtained *via* deconvolution with a Randle-type equivalent-circuit model (Fig. S10†).[46–48] The equivalent-circuit model describes the electrochemical reaction steps, including Na-ion migration through solid–electrolyte interphase (SEI) layers, a charge-transfer reaction, and Na-ion diffusion kinetics throughout the active materials.[49–51] The medium-frequency semicircles in the Nyquist plots shown in Fig. 6 are attributed to the charge-transfer resistance (R_{ct}) between the active material and the electrolyte, while the low-frequency region corresponds to the diffusion of Na within the electrodes.[52–54] All of the samples exhibit similar R_{ct} values before cycling, as shown in Fig. 6a. Fig. 6b shows the relationship between Z_{re} and $\omega^{-1/2}$ in the low-frequency region, where ω is the angular frequency in the low-frequency region ($\omega = 2\pi f$).[55] The lower gradient in the low-frequency region of the C@$MoTe_2$ plot indicates that the Na-ion diffusivity in the C@$MoTe_2$ composite microspheres is higher

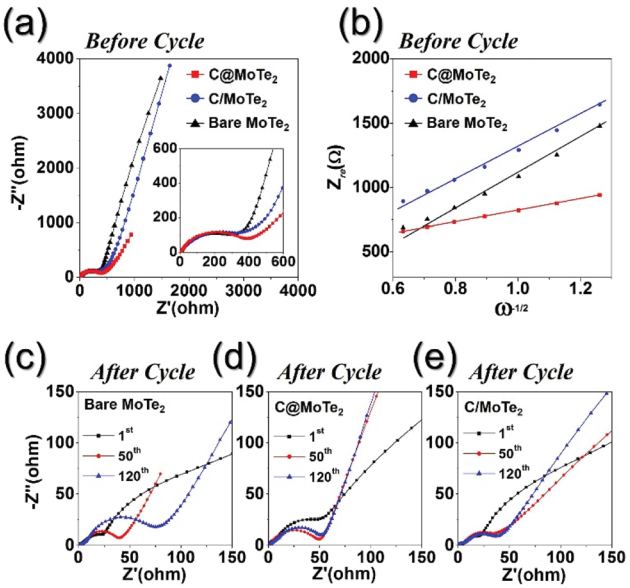

Fig. 6 (a, c, d, e) Nyquist impedance plots and (b) relationships between the real part of the impedance (Z_{re}) and $\omega^{-1/2}$ of the C@$MoTe_2$ and C/$MoTe_2$ composite microspheres and bare $MoTe_2$ powders before and after cycling.

than that of the other samples.[55] The thin $MoTe_2$ shell covering the C microsphere is responsible for the higher Na-ion diffusivity of the C@$MoTe_2$ composite microspheres compared to that of the other structures. The R_{ct} values of the three samples decrease abruptly after the first cycle, which is due to the transformation of the $MoTe_2$ crystals into ultrafine nanocrystals during the first cycle.[42,43] The R_{ct} values of the bare $MoTe_2$ powder steadily increase during cycling (Fig. 6c), which is because of the structural destruction due to the repeated Na-ion sodiation and desodiation processes. The R_{ct} values of the bare $MoTe_2$ powder before cycling and after 1, 50, and 120 cycles are 427, 31, 43, and 84 Ω, respectively. On the other hand, the R_{ct} values of the C@$MoTe_2$ and C/$MoTe_2$ microspheres are almost identical over the 120 cycles, as shown in Fig. 6d and e, respectively. The R_{ct} values of both the C@$MoTe_2$ and C/$MoTe_2$ cells after 120 cycles are 52 and 41 Ω, respectively. The results of the EIS analysis are evidence of the structural stability of the C@$MoTe_2$ and C/$MoTe_2$ microspheres during the repeated sodiation and desodiation processes. The presence of C in the C@$MoTe_2$ and C/$MoTe_2$ microspheres improves the structural stability of the samples because of the robust composite structure. Finally, the high structural stability and well-developed 2D layer of $MoTe_2$ of the C@$MoTe_2$ microspheres provide superior Na-ion storage properties compared to those of the C/$MoTe_2$ microspheres and bare $MoTe_2$ powder.

Conclusions

In this study, $MoTe_2$ materials with and without carbonaceous materials have been applied for the first time as anode

materials in NIBs. The C–$MoTe_2$ composite microspheres with two different morphologies were prepared *via* the tellurization of C–MoO_x composite microspheres at different temperatures. The core–shell-structured C@$MoTe_2$ microspheres, which were formed by an Ostwald ripening process, exhibited excellent Na-ion storage properties compared to those of the C/$MoTe_2$ microspheres and bare $MoTe_2$ powders. Nanostructured $MoTe_2$ materials with a large Te–Mo–Te interlayer spacing of 0.699 nm appear to be a promising anode material for NIBs.

Acknowledgements

This work was supported by a National Research Foundation of Korea (NRF) grant funded by the Korea government (MEST) (NRF-2015R1A2A1A15056049). This work was supported by the Energy Efficiency & Resources Core Technology Program of the Korea Institute of Energy Technology Evaluation and Planning (KETEP), granted financial resource from the Ministry of Trade, Industry & Energy, Republic of Korea (201320200000420 and 20153030091450).

Notes and references

1 S. Z. Butler, S. M. Hollen, L. Cao, Y. Cui, J. A. Gupta, H. R. Gutiérrez, T. F. Heinz, S. S. Hong, J. Huang and A. F. Ismach, *ACS Nano*, 2013, **7**, 2898–2926.
2 M. Chhowalla, H. S. Shin, G. Eda, L.-J. Li, K. P. Loh and H. Zhang, *Nat. Chem.*, 2013, **5**, 263–275.
3 G. Fiori, F. Bonaccorso, G. Iannaccone, T. Palacios, D. Neumaier, A. Seabaugh, S. K. Banerjee and L. Colombo, *Nat. Nanotechnol.*, 2014, **9**, 768–779.
4 Q. H. Wang, K. Kalantar-Zadeh, A. Kis, J. N. Coleman and M. S. Strano, *Nat. Nanotechnol.*, 2012, **7**, 699–712.
5 M. Xu, T. Liang, M. Shi and H. Chen, *Chem. Rev.*, 2013, **113**, 3766–3798.
6 Y. G. Guo, J. S. Hu and L. J. Wan, *Adv. Mater.*, 2008, **20**, 2878–2887.
7 T. Stephenson, Z. Li, B. Olsen and D. Mitlin, *Energy Environ. Sci.*, 2014, **7**, 209–231.
8 D. Voiry, M. Salehi, R. Silva, T. Fujita, M. Chen, T. Asefa, V. B. Shenoy, G. Eda and M. Chhowalla, *Nano Lett.*, 2013, **13**, 6222.
9 H. Wang, H. Feng and J. Li, *Small*, 2014, **10**, 2165–2181.
10 E. Yang, H. Ji and Y. Jung, *J. Phys. Chem. C*, 2015, **119**, 26374.
11 Y. You, X. L. Wu, Y. X. Yin and Y. G. Guo, *Energy Environ. Sci.*, 2014, **7**, 1643–1647.
12 M. S. Islam and C. A. J. Fisher, *Chem. Soc. Rev.*, 2014, **43**, 185–204.
13 W. Li, Z. Yang, M. Li, Y. Jiang, X. Wei, X. Zhong, L. Gu and Y. Yu, *Nano Lett.*, 2016, **16**, 1546–1553.
14 B. Qu, C. Ma, G. Ji, C. Xu, J. Xu, Y. S. Meng, T. Wang and J. Y. Lee, *Adv. Mater.*, 2014, **26**, 3854–3859.
15 M. D. Slater, D. Kim, E. Lee and C. S. Johnson, *Adv. Funct. Mater.*, 2013, **23**, 947–958.
16 J. S. Cho, J.-K. Lee and Y. C. Kang, *Sci. Rep.*, 2016, **6**, 23699.
17 J. S. Cho, S. Y. Lee and Y. C. Kang, *Sci. Rep.*, 2016, **6**, 23338.
18 K. Zhang, Z. Hu, X. Liu, Z. Tao and J. Chen, *Adv. Mater.*, 2015, **27**, 3305–3309.
19 T. Zhou, W. K. Pang, C. Zhang, J. Yang, Z. Chen, H. K. Liu and Z. Guo, *ACS Nano*, 2014, **8**, 8323–8333.
20 G. D. Park and Y. C. Kang, *Chem. – Eur. J.*, 2016, **22**, 4140–4146.
21 L. David, R. Bhandavat and G. Singh, *ACS Nano*, 2014, **8**, 1759–1770.
22 H. Wang, X. Lan, D. Jiang, Y. Zhang, H. Zhong, Z. Zhang and Y. Jiang, *J. Power Sources*, 2015, **283**, 187–194.
23 Y. N. Ko, S. H. Choi, S. B. Park and Y. C. Kang, *Nanoscale*, 2014, **6**, 10511–10515.
24 C. Zhu, X. Mu, P. A. van Aken, Y. Yu and J. Maier, *Angew. Chem., Int. Ed.*, 2014, **53**, 2152–2156.
25 N. R. Pradhan, D. Rhodes, S. Feng, Y. Xin, S. Memaran, B.-H. Moon, H. Terrones, M. Terrones and L. Balicas, *ACS Nano*, 2014, **8**, 5911–5920.
26 M. Yamamoto, S. T. Wang, M. Ni, Y.-F. Lin, S.-L. Li, S. Aikawa, W.-B. Jian, K. Ueno, K. Wakabayashi and K. Tsukagoshi, *ACS Nano*, 2014, **8**, 3895–3903.
27 Y. F. Lin, Y. Xu, S. T. Wang, S. L. Li, M. Yamamoto, A. Aparecido-Ferreira, W. Li, H. Sun, S. Nakaharai and W. B. Jian, *Adv. Mater.*, 2014, **26**, 3263–3269.
28 C. Ruppert, O. B. Aslan and T. F. Heinz, *Nano Lett.*, 2014, **14**, 6231–6236.
29 T. Anand and N. H. Mazlan, *Adv. Mater. Res.*, 2014, **845**, 392–397.
30 J. Kang, S. Tongay, J. Zhou, J. Li and J. Wu, *Appl. Phys. Lett.*, 2013, **102**, 012111.
31 D. Kong, H. Wang, J. J. Cha, M. Pasta, K. J. Koski, J. Yao and Y. Cui, *Nano Lett.*, 2013, **13**, 1341–1347.
32 A. Ramasubramaniam, *Phys. Rev. B: Condens. Matter*, 2012, **86**, 115409.
33 P. Tonndorf, R. Schmidt, P. Böttger, X. Zhang, J. Börner, A. Liebig, M. Albrecht, C. Kloc, O. Gordan and D. R. Zahn, *Opt. Express*, 2013, **21**, 4908–4916.
34 J. C. Bernède, C. Amory, L. Assmann and M. Spiesser, *Appl. Surf. Sci.*, 2003, **219**, 238–248.
35 L. Zhou, K. Xu, A. Zubair, A. D. Liao, W. Fang, F. Ouyang, Y.-H. Lee, K. Ueno, R. Saito and T. Palacios, *J. Am. Chem. Soc.*, 2015, **137**, 11892–11895.
36 X. Xiong, W. Luo, X. Hu, C. Chen, L. Qie, D. Hou and Y. Huang, *Sci. Rep.*, 2015, **5**, 9254.
37 H. Bando, K. Koizumi, Y. Oikawa, K. Daikohara, V. A. Kulbachinskii and H. Ozaki, *J. Phys.: Condens. Matter*, 2000, **12**, 5607–5616.
38 M.-C. Lin, M. Gong, B. Lu, Y. Wu, D.-Y. Wang, M. Guan, M. Angell, C. Chen, J. Yang and B.-J. Hwang, *Nature*, 2015, **520**, 324–328.
39 G. D. Park, J. S. Cho and Y. C. Kang, *Nano Energy*, 2015, **17**, 17–26.

40 X. Zhang, Y. Jiao, L. Sun, L. Wang, A. Wu, H. Yan, M. Meng, C. Tian and B. Jiang, *Nanoscale*, 2015, **8**, 2418–2427.
41 A. C. Ferrari, J. C. Meyer, V. Scardaci, C. Casiraghi, M. Lazzeri, F. Mauri, S. Piscanec, D. Jiang, K. S. Novoselov and S. Roth, *Phys. Rev. Lett.*, 2006, **97**, 187401.
42 J. S. Cho, J. M. Won, J.-H. Lee and Y. C. Kang, *Nanoscale*, 2015, **7**, 19620–19626.
43 Y. Sun, X. Hu, W. Luo, F. Xia and Y. Huang, *Adv. Funct. Mater.*, 2013, **23**, 2436–2444.
44 D. Kong, H. He, Q. Song, B. Wang, W. Lv, Q.-H. Yang and L. Zhi, *Energy Environ. Sci.*, 2014, **7**, 3320–3325.
45 Y. Shi, C. Hua, B. Li, X. Fang, C. Yao, Y. Zhang, Y.-S. Hu, Z. Wang, L. Chen, D. Zhao and G. D. Stucky, *Adv. Funct. Mater.*, 2013, **23**, 1832–1838.
46 J. S. Cho, Y. J. Hong, J.-H. Lee and Y. C. Kang, *Nanoscale*, 2015, **7**, 8361–8367.
47 J. S. Cho and Y. C. Kang, *Small*, 2015, **11**, 4673–4681.
48 D. T. Ngo, R. S. Kalubarme, H. T. T. Le, J. G. Fisher, C. N. Park, I. D. Kim and C. J. Park, *Adv. Funct. Mater.*, 2014, **24**, 5291–5298.
49 H. Wu, M. Xu, Y. Wang and G. Zheng, *Nano Res.*, 2013, **6**, 167–173.
50 H. Wu, M. Xu, H. Wu, J. Xu, Y. Wang, Z. Peng and G. Zheng, *J. Mater. Chem.*, 2012, **22**, 19821–19825.
51 L. Yunjian, L. Xinhai, G. Huajun, W. Zhixing, H. Qiyang, P. Wenjie and Y. Yong, *J. Power Sources*, 2009, **189**, 721–725.
52 J. S. Cho, Y. J. Hong and Y. C. Kang, *ACS Nano*, 2015, **9**, 4026–4035.
53 Z. Wang, D. Luan, S. Madhavi, Y. Hu and X. W. D. Lou, *Energy Environ. Sci.*, 2012, **5**, 5252–5256.
54 Y. Xu, Y. Zhu, Y. Liu and C. Wang, *Adv. Energy Mater.*, 2013, **3**, 128–133.
55 G. Q. Liu, H. T. Kuo, R. S. Liu, C. H. Shen, D. S. Shy, X. K. Xing and J. M. Chen, *J. Alloys Compd.*, 2010, **496**, 512–516.